processes

MDPI

Article

Thermo-Mechanically Coupled Settlement and Temperature Response of a Composite Foundation in Complex Geological Conditions for Molten Salt Tank in Tower Solar Plants

Shezhou Zhu [1], Xu Li [1], Yi Li [2,*], Hemei Sun [2] and Xin Kang [2,*]

[1] Shandong Electric Power Engineering Consulting Institute Co., Ltd., Jinan 524447, China; zhushezhou@sdepci.com (S.Z.); lixu@sdepci.com (X.L.)
[2] College of Civil Engineering, Hunan University, Changsha 410082, China; sunhemei@hnu.edu.cn
* Correspondence: yili0401@hnu.edu.cn (Y.L.); kangxin@hnu.edu.cn (X.K.); Tel.: +86-15079515641 (Y.L.); +86-18392218715 (X.K.)

Abstract: The degradation of complex geological structures due to thermo-mechanical cycling results in a reduction in bearing capacity, which can readily induce engineering issues such as uneven settlement, cracking, and even the destabilization of the foundations of molten salt storage tanks. This study establishes a foundational model for a molten salt storage tank through the use of COMSOL Multiphysics and conducts a numerical simulation analysis to evaluate the settlement deformation and temperature distribution of the foundation under the influence of thermo-mechanical coupling. Concurrently, the research proposes two distinct design approaches for the tank's foundational structure. A comparative analysis of the results indicates that the use of a pile raft foundation in conjunction with a traditional foundation mode results in a reduction of settlement at the center of the foundation's top surface by 380.1 mm, while also decreasing the maximum effective stress in the steel ring wall by 240.7 MPa. The thermal effects impact a depth of 10 m in the foundation soil and an influence radius of 20 m. Additionally, the foundation soil exhibits optimal thermal insulation properties, resulting in minimal energy loss. These findings indicate that the pile raft foundation in conjunction with a traditional foundation mode displays remarkable adaptability to complex geological conditions, with both settlement and temperature distribution of the foundation maintained within acceptable limits.

Keywords: complex geology; thermo-mechanical coupling; molten salt storage tank foundation; settlement deformation; temperature distribution

check for updates

Citation: Zhu, S.; Li, X.; Li, Y.; Sun, H.; Kang, X. Thermo-Mechanically Coupled Settlement and Temperature Response of a Composite Foundation in Complex Geological Conditions for Molten Salt Tank in Tower Solar Plants. *Processes* **2024**, *12*, 2602. https://doi.org/10.3390/pr12112602

Academic Editor: Paola Ammendola

Received: 29 September 2024
Revised: 9 October 2024
Accepted: 18 November 2024
Published: 19 November 2024

Copyright: © 2024 by the authors. Licensee MDPI, Basel, Switzerland. This article is an open access article distributed under the terms and conditions of the Creative Commons Attribution (CC BY) license (https://creativecommons.org/licenses/by/4.0/).

1. Introduction

Energy supply is a paramount issue, with particular public concern over greenhouse gas emissions and the necessity to reduce the utilization of fossil fuels [1]. According to current statistics and forecasts of energy consumption, the U.S. Energy Information Administration predicts that the global total energy use will increase from 0.15×10^{12} MWh in 2008 to 0.18×10^{12} MWh by 2020 and further rise to 0.23×10^{12} MWh by 2035 [2]. The escalation in energy consumption correlates with an increase in carbon dioxide emissions, necessitating maximizing CO_2 absorption through carbon sequestration by both natural means and by technical developments and the development of highly efficient energy capture, storage and re-use methods [3,4]. Amidst the global energy paradigm shift towards sustainable practices and the imperative for low-carbon environmental protection, photovoltaic (PV) energy generation emerges as a pivotal clean energy source. It is instrumental in facilitating the transition towards a low-carbon economy and in hastening the realization of the ambitious carbon neutrality benchmarks [5]. As of the year 2024, the electric power generation capacity in China has escalated to approximately 9.96 trillion kilowatt-hours, with the installed non-fossil-fuel energy generation capacity witnessing a significant upsurge, now constituting roughly 55% of the

total energy mix. The contribution of wind and solar power to the national energy generation portfolio has surpassed 17%, marking a significant stride in the realm of clean and efficient energy development and utilization [6]. In the continuum of renewable energy technologies, molten salt energy storage stands out as an innovative solution that enhances the reliability of photovoltaic power plants. This technology enables the provision of a continuous and stable energy output, even in the absence of solar irradiation, such as during nocturnal periods or under overcast and inclement weather conditions. It effectively mitigates the intermittency issues associated with solar energy and the variability of meteorological conditions, thereby offering the critical advantage of a dispatchable and uninterrupted power supply [7]. This attribute is of paramount importance for the stability of power grid operations and for diminishing the reliance on conventional fossil-fuel-based generation methods. In terms of energy consciousness, thermal energy storage (TES) systems are becoming increasingly significant, as TES can reduce the Levelized Cost of Electricity (LCOE) in renewable energy processes [8]. Furthermore, energy storage allows for the adjustment of the grid scale to more closely align with average energy flow rather than peak power demands, while reducing transmission losses and enhancing the stability and reliability of the power grid. This plays a crucial role in transitioning towards more efficient and sustainable energy utilization [8,9].

Molten salt storage tanks, serving as the pivotal component within the ambit of molten salt energy storage technology, are highly esteemed for their exceptional efficacy in the sequestration and conveyance of high-temperature media. These tanks, typically cylindrical in configuration, are comprised of three principal constituents: the metallic tank wall, the insulative material, and the substructural foundation [10]. Gabbrielli R. et al. have demonstrated a substantial reduction of approximately 20% in the production costs relative to conventional stainless steel tanks by employing insulated carbon steel as the primary material for the tank wall [11]. Gasia J. et al. have conducted an exhaustive review of high-temperature thermal energy storage systems and materials, encompassing a multiplicity of perspectives [12]. Molten salts have emerged as the quintessential medium for thermal energy storage within thermal energy storage (TES) systems, a status underpinned by their substantial heat capacity, reduced melting point, and relatively stable thermophysical properties [13,14]. However, the propensity for molten salts to exert a corrosive influence on storage tanks at elevated temperatures is a factor that warrants vigilant attention. For instance, chloride salts have been observed to exhibit an erosion rate surpassing 300 μm per annum [15]. Gomez-Vidal J.C. et al. have illustrated that boron nitride coatings can significantly impede the permeation of molten chlorides into metallic substrates. Nevertheless, further research is imperative to evaluate the long-term chemical stability of such protective coatings [16]. In a study undertaken by Muhammad T.M. et al., engineered concrete composites were developed through the incorporation of admixtures and coatings. These composites have been found to be more economically viable than traditional approaches and have demonstrated an ability to curtail the permeation of molten salts through porous concrete matrices. This discovery holds profound implications for the application of such composites in the construction of storage tank infrastructure [17,18]. Gomez-Villarejo R. et al. have synthesized and deployed nanofluids as an alternative to molten salts in their capacity as thermally conductive fluids, with results indicating that nanofluids possess superior thermal characteristics [19].

In the realm of thermal energy storage (TES) systems, the foundation of the molten salt storage tank emerges as a pivotal structural element, with its geometric attributes, including height and dimensions, exerting a profound influence on the overall system's stability and safety [20]. Torras S. et al. have conducted a seminal study that delineates three critical parameters intrinsic to the efficacy of TES systems: meteorological data, the insulation thickness of the storage tanks, and the structure of the tank foundations, underscoring the significant role of the latter [21]. Zhou H. et al. have introduced an innovative tank foundation design incorporating road base materials, lightweight expanded clay aggregate (LECA), thermal clay blocks, and refractory bricks as insulating agents [7]. This novel approach has been demonstrated to enhance the thermal performance of the

tank foundation, thereby curtailing heat loss emanating from the tank foundation. Zhang X.M. et al. have constructed an experimental TES system utilizing a novel molten salt as the energy storage medium, which has facilitated the measurement of temperature gradients across the insulated foundation. Their findings reveal that the apex of temperature is localized in the upper central region of the foundation, with a radial decrease in temperature profiles [22]. In the quest to regulate the temperature distribution within molten salt storage tanks, the selection of thermal insulation materials and the implementation of heat dissipation strategies are of paramount importance. Wan Z.J. et al. have proposed a coupled thermal performance assessment model designed to evaluate heat loss and temperature distribution within molten salt storage tanks. Their research highlights that, in the absence of a cooling mechanism, the elevated temperature of the molten salt can significantly influence the temperature of the tank foundations, particularly the soil at the base, potentially jeopardizing the safe operation of the TES system [10]. This underscores the indispensable nature of a cooling system for molten salt storage tanks. Rodríguez I. et al. have advocated for a parallel modular approach to the modeling of molten salt storage tanks. This methodology treats the tank walls, foundations, insulation materials, and molten salt media as distinct systems, employing varying degrees of modeling sophistication. These systems are then interconnected via boundary conditions, and they assessed the operational temperatures of the passive cooling systems of the molten salt tanks, noting that the temperature of the reinforced concrete comprising the tank foundations should not surpass 90 °C [23]. Schulte-Fischedick J. et al. have modeled a two-tank 880MWh energy storage system and employed the finite element method (FEM) to calculate heat loss. Their analysis indicates that significant heat loss fluxes occur at the interface between the sidewalls and the bottom plate of the molten salt tank [24]. Consequently, the design considerations pertaining to the lower edge of the molten salt storage tank are of considerable consequence to the overall heat loss.

Yang X.P. et al. have delved into the experimental investigation of the thermocline heat transfer phenomena within molten salt storage tanks, utilizing molten salt as the heat transfer medium and ceramic particles as the filler material [25]. Zhou H et al. have independently crafted a hot-wire instrument to probe the effective thermal conductivity of stacked ceramic grains, varying in grain size, density, and porosity [13]. Their findings reveal a robust linear correlation between the effective thermal conductivity and the density and porosity of the ceramic stacks. This correlation is of significant import for the selection of particle size and gradation in base insulation materials and the engineering design of tank foundations. Furthermore, Zhou H et al. have also examined the thermal stability, pore structure, thermal conductivity, permeability, and compressive resistance of stacked ceramic grains [26]. Their results underscore the ceramic grains' commendable thermal properties, minimal permeability, and ample compressive strength, rendering them an exemplary insulating material for tank foundations. Xia Z. et al. have ventured into the thermodynamic properties of five sand-kaolin binary soil mixtures, spanning a sand content gradient from 0% to 100% [27]. Their study discerns the presence of a sand content threshold that bifurcates the trend of thermodynamic properties into three distinct categories. Consequently, a more generalized K-model has been formulated to prognosticate the thermodynamic properties of these binary soil mixtures. Kang X. et al. have introduced an enhanced one-dimensional series-parallel (S-II) thermal conductivity model tailored for estimating the thermal conductivity of class C fly ash over time [28,29]. The model's feasibility has been experimentally substantiated, providing a crucial reference for the reinforcement of tank foundations and for understanding the temporal dynamics of the thermal conductivity of foundation soils.

Gabbrielli R et al. have formulated an optimization protocol for the design of molten salt storage tanks, taking into account a triad of critical factors: thermal, mechanical, and economic [11]. Given the elevated operating temperatures of molten salt storage tanks, which can now reach 600 °C [30], there exist a paucity of design codes specifically tailored for such high-temperature thermal storage applications. Traditional design codes, such as

API Standard 650, which is prevalent in the petrochemical industry and has a maximum design temperature of 260 °C [31], have been employed in the absence of specific guidelines [10]. However, this standard is not optimized for higher temperatures, necessitating further research into tank design. Liang T. et al. have conducted a multi-field coupling analysis of the foundation of molten salt tanks under general geological conditions, demonstrating the adaptability of traditional tank foundations [32]. Nonetheless, in geologically complex settings, such as weak geological, the interaction of thermal and mechanical stress cycles can compromise the foundation's structural integrity, potentially leading to settlement, cracking, or even catastrophic failure. To address these challenges, Tian Q. et al. have proposed a composite foundation design that enhances the load-bearing capacity and stability by incorporating a reinforced concrete layer at the base and have introduced the concept of pile foundations tailored to specific geological conditions [33].

In response to the aforementioned issue, this study integrates the structural design of the storage tank foundation for a tower-mounted photovoltaic power plant situated in Xinjiang. Utilizing COMSOL Multiphysics, a computational platform, a foundational model for the molten salt storage tank has been meticulously constructed. Subsequently, finite element analysis was conducted to evaluate the performance of the traditional foundation under the combined effects of thermal and mechanical stressors. Building upon these findings, this research introduces two innovative foundation design methodologies tailored for molten salt storage tanks capable of withstanding the complexities of diverse geological settings. These proposals are intended to serve as a benchmark for the design of storage tank foundations in analogous geological contexts in future endeavors.

2. Geological Conditions

2.1. Stratigraphic Lithology

The stratigraphic sequence revealed by the exploratory survey of this project, in descending order, comprises the Quaternary Holocene alluvial deposits (Q_4^{al+pl}), characterized by a stratum of pulverized clay, silt, and medium-coarse sand. The absence of groundwater during the survey indicates that the aquifer is located at significant depths beneath the site. Consequently, the potential influence of groundwater on the structural integrity of the foundation can be deemed negligible. The lithological composition and stratigraphic distribution of the strata are delineated as follows.

Layer of Silty Clay (Q_4^{al+pl}): Resulting from alluvial, this stratum presents a color gradient from gray-yellow to gray-brown. It exhibits a texture that transitions from medium-hard to plastic, indicative of moderate compressibility. This soil horizon is consistently encountered at a depth of 9.0 m across the survey area.

Layer of Silt (Q_4^{al+pl}): A product of alluvial processes, this stratum is predominantly gray-yellow in color. It is characterized by a loose texture, high saturation, and a composition primarily of well-sorted, pure sand grains. The mineralogy is predominantly quartz and feldspar. This stratum is consistently encountered between depths of 9.0 and 20.0 m, with an average thickness of 7.0 m.

Layer of Medium-Coarse Sand (Q_4^{al+pl}): This sand layer, also a product of alluvial processes, is gray-yellow and exhibits a medium-dense texture. It is saturated and composed of well-sorted, pure sand grains with a mineralogy dominated by quartz and feldspar. This stratum is laterally consistent within the survey area, with thicknesses varying from 10.0 to 18.0 m and an average thickness of 15.0 m.

Layer of Silty Clay (Q_4^{al+pl}): This silty clay layer is a result of alluvial. It displays a coloration from gray-yellow to gray-brown, with a texture that is medium-hard to plastic, and it exhibits moderate compressibility. This layer is laterally stable within the survey area.

2.2. The Soil Mechanics Parameters for Each Stratum of Soil

Based on the findings from the field reconnaissance, the geotechnical parameters of each stratum are delineated in Table 1.

Table 1. Geotechnical properties of each soil layer.

Soil Layer	Weight (kN/m^3)	Cohesion (kPa)	Angle of Internal Friction (°)	Compression Modulus (MPa)	Bearing Capacity (kPa)
① Layer of silty clay (Q_4^{al+pl})	19.0	4.2	16.3	7.0	120
② Layer of silt (Q_4^{al+pl})	22.0	0	22.0	5.0	200
③ Layer of medium-coarse sand (Q_4^{al+pl})	24.0	0	20.0	15.0	350
④ Layer of silty clay (Q_4^{al+pl})	20.0	7.2	19.0	6.8	160

3. Materials and Methods

This section offers an exhaustive overview of the foundation model for a molten salt storage tank, with a detailed exposition of the research methodology, commencing with the foundation design, providing an in-depth description of the foundation structure and material parameters, and followed by a discussion on the software employed, the selection of boundary conditions, the establishment of the model, and the discretization of the mesh, which are a series of procedural steps in simulation computation.

3.1. Foundation Design

Given the complex geological conditions at the site of the tower-type photovoltaic power plant, the foundation-bearing capacity is inherently limited. Utilizing the traditional design for a molten salt storage tank foundation would result in excessive settlement and inadequate load-bearing capacity. Consequently, two foundation design approaches are proposed: a composite foundation in conjunction with a traditional foundation mode, and a pile raft foundation in conjunction with a traditional foundation mode. For the composite foundation combined with traditional foundations, considering the depth and thickness of the weak-bearing-capacity silty clay layer within the foundation soil, the traditional foundation is underpinned with immersed pipe gravel piles to create a composite foundation. The gravel piles are designed with a diameter of 0.5 m and a length of 15 m, arranged in a square pattern with a pile spacing of 1.5 m. At the periphery of the traditional foundation, four rows of piles are extended, and the pile tops are capped with a 0.5-m-thick crushed stone bedding layer, with the bedding radius set at 30 m [34]. For the pile raft foundation combined with traditional foundations, in light of the stress conditions of the storage tank foundation, a flat plate raft foundation is specified with a thickness of 1 m and a radius of 18 m. Precast piles are installed beneath the raft foundation, with a length of 15 m, a diameter of 0.6 m, and arranged in a square pattern with a pile spacing of 3.5 m [35]. Both the raft slab and the piles are constructed using heat-resistant concrete.

The traditional foundation form is depicted in Figure 1. Under normal operating conditions, the molten salt storage tank foundation is subjected to a combination of loads, including thermal. In accordance with the design of this molten salt storage tank, the tank load should be calculated based on the quantity of molten salt required for a 12-h heat storage duration; i.e., each molten salt tank should be loaded with at least 29,500 metric tons of molten salt to account for the foundation load. The tank body, inclusive of accessories, weighs 700 metric tons. The operating temperature of the high-temperature tank ranges from 525 to 535 °C, with a design temperature set at 550 °C.

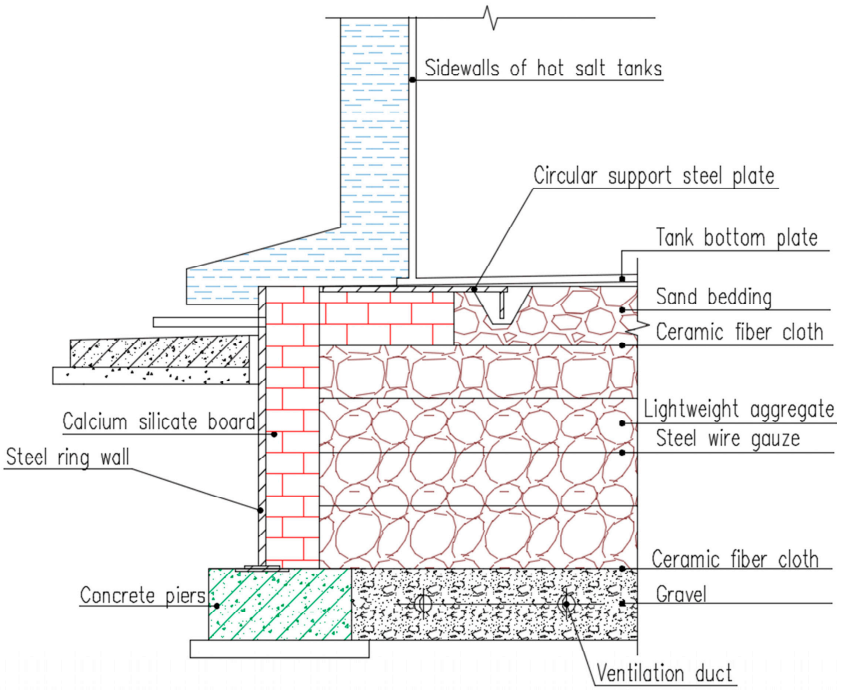


Figure 1. Traditional foundation of a molten salt storage tank.

3.2. Structural and Material Parameters of Foundation

The foundation structure of the molten salt storage tank is comprised of two primary components: the load-bearing structure and the insulation structure. The load-bearing structure encompasses refractory concrete blocks, steel ring walls, concrete piers, and concrete pads. Refractory concrete blocks, with a compressive strength of not less than 2.5 MPa, are tasked with bearing the load transmitted from the tank's upper extremity. These blocks are 800 mm in width and 300 mm in thickness. The steel ring wall serves to confine the lateral displacement of the insulation material, thereby preventing excessive settlement of the storage tank. It measures 30 mm in thickness and 1550 mm in height. Both concrete piers and pads are cast using C30 concrete. The piers are 800 mm wide and 400 mm high, while the pads are 1000 mm wide and 150 mm thick. These elements are designed to mitigate the risk of differential settlement and to preclude stress concentration that could arise from direct contact between the steel ring wall and the underlying soil. The insulation structures consist of a sand bedding layer, lightweight aggregate, calcium silicate board, and a fine gravel layer. The sand bedding, made from fine sand and 300 mm thick, provides a flexible support base for the tank's bottom plate, accommodating the necessary deformations. The primary insulating components are composed of lightweight aggregate and calcium silicate board. The lightweight aggregate is graded to meet specific requirements, with a maximum particle size not exceeding 19 mm, a compressive strength of at least 1.2 MPa, and a thickness of 1250 mm. Calcium silicate boards are positioned on either side of the lightweight aggregate, boasting a heat resistance of at least 600 °C, with dimensions of 300 mm in thickness and 1550 mm in height. The fine gravel layer is 400 mm thick and incorporates embedded ventilation pipes to ensure adequate airflow and heat dissipation at the foundation's base. Furthermore, we have conducted experimental simulations to determine the thermal conductivity of the lightweight aggregate and calcium silicate board under operational conditions, facilitating a precise analysis of the temperature distribution within the tank foundation. The detailed parameters for each material are presented in Table 2.

Table 2. Model parameters of each material.

Parameters	Refractory Brick	Concrete Pier	Steel Ring Wall	Sand Cushion	Lightweight Aggregate	Calcium Silicate Board	Pea Gravel
Density (kg/m^3)	2200	2400	7900	1600	550	1600	2100
Cohesion (kPa)	-	-	-	0	0	-	0
Angle of internal friction (°)	-	-	-	30	10	-	35
Compression modulus (MPa)	30,000	30,000	200,000	30	35	20,000	35
Poisson's ratio	0.2	0.15	0.3	0.3	0.3	0.2	0.3
Tensile strength (MPa)	1.43	1.43	-	-	-	10	-
Compressive strength (MPa)	14.3	14.3	-	-	-	35	-
Biaxial compressive strength (MPa)	16	16	-	-	-	38	-
Thermal conductivity (W/(m·K))	0.2	1.5	45	0.9	0.25	0.12	1.1
Heat capacity (J/(kg·K))	880	1000	500	800	2000	780	1000
Coefficient of thermal expansion (1/K)	1×10^{-5}	1×10^{-5}	1.2×10^{-5}	4×10^{-6}	1×10^{-6}	1×10^{-5}	4×10^{-6}

3.3. Software Introduction

COMSOL Multiphysics 6.1 is a robust interactive simulation software designed for modeling and resolving diverse scientific and engineering challenges. It specializes in multiphysics modeling, enabling users to expand from single-physics models to multiphysics models that address coupled physical phenomena concurrently. COMSOL Multiphysics is founded on the finite element method, facilitating the simulation of real physical phenomena through the solution of partial differential equations for individual fields or systems of partial differential equations for multiple interacting fields. The software's integrated physics interfaces and sophisticated material property support allow users to construct models by defining pertinent physical quantities, such as material attributes, loadings, and constraints, without the necessity of specifying the underlying equations. These variables, expressions, or numerical values can be directly applied to solid and fluid domains, boundaries, edges, and nodes, irrespective of the computational mesh. The software has been extensively utilized in various domains, including acoustics, fluid dynamics, thermal conduction, optics, and structural mechanics [36].

3.4. The Constitutive Model of Foundation Materials

3.4.1. Drucker–Prager Criterion

The Drucker–Prager criterion, a yield function utilized in geotechnical engineering, delineates the stress-strain behavior of materials, including soils and rocks. This model ascertains the material's strength envelope through a biparametric assessment, quantifying both the material's cohesion and the angle of internal friction, as illustrated by the following equation:

$$\alpha = \frac{2}{\sqrt{3}} \bullet \frac{\sin \varphi}{3 \pm \sin \varphi} \tag{1}$$

$$k = \frac{2\sqrt{3} c \cos \varphi}{3 \pm \sin \varphi} \tag{2}$$

where c is the cohesion and φ is the angle of internal friction.

The Drucker–Prager criterion more effectively characterizes the plastic deformation behavior of soils and accommodates multiaxial stress states. In contrast to the Mohr–Coulomb criterion, which is confined to the principal stress plane, the Drucker–Prager

model incorporates the concept of a flow surface, thereby extending its applicability to arbitrary stress paths. The mathematical formulation of the criterion is relatively straightforward, facilitating its implementation within finite element analyses. This criterion has been employed to model the sand bedding layers, lightweight aggregate, fine gravel, and the foundation soil in foundation designs.

3.4.2. Bresler–Pister Criterion

The Bresler–Pister criterion, a robust criterion for material strength predicated on the quantification of average stress states, predominantly serves to assess the onset of yielding or the incipient stages of material degradation. Initially formulated to prognosticate the strength envelope of concrete subjected to multiaxial stress regimens, this criterion encompasses parameters such as uniaxial compressive strength, uniaxial tensile strength, and biaxial compressive strength, which collectively delineate the commencement of concrete damage under triaxial stress conditions, as illustrated by the following equation:

$$\frac{\tau_{oct}}{f_c'} = a - b\frac{\sigma_{oct}}{f_c'} + c\left(\frac{\sigma_{oct}}{f_c'}\right)^2 \quad (3)$$

where, a, b, and c coefficients can be derived from uniaxial compressive strength, uniaxial tensile strength, and biaxial compressive strength test data.

The Bresler–Pister criterion was used for refractory bricks, concrete piers and pads, and calcium silicate boards in foundations.

3.5. Model Establishment

In light of the axisymmetric characteristics of the tank foundation's geometry, load distribution, and temperature distribution, a two-dimensional axisymmetric approach has been adopted to construct the geometric model. This methodology effectively transforms the intricate three-dimensional problem into a more tractable two-dimensional representation, thereby significantly reducing the complexity of the model and expediting the computational process. To mitigate the impact of the foundation soil boundary on the analysis outcomes, the extent of the foundation soil has been maximized. In this study, the radius of the foundation soil is delineated as 100 m, with a depth of 50 m. The remaining sections of the model are constructed in accordance with the structural parameters of the foundation (Section 3.2). For the pile raft foundation combined with a traditional foundation model, due to the inherent incompatibility between concrete pile and soil calculations within the multiphysics domain, the region where the pile foundation is distributed in the model is treated as a soil body with an equivalent elastic modulus. This soil body is characterized by an equivalent area thickness of 15 m and a radius of 18 m, drawing upon the equivalent action surface method for calculating the settlement of pile foundations [35]. The modulus of elasticity for reinforced concrete is specified as 3×10^4 MPa. Given that the pile bottom area constitutes 2.7% of the bottom area of the equivalent area, the modulus of elasticity of the equivalent soil body is accordingly set to 2.7% of that of reinforced concrete, which equates to 808 MPa. The final geometric model is depicted in Figure 2.

3.6. Boundary Conditions and Load and Temperature Field Settings

3.6.1. Boundary Conditions

The base of the foundation soil is designated as a fully fixed constraint, thereby precluding any displacements and ensuring stability. Conversely, the sidewalls are modeled as roller supports, which permit unidirectional vertical displacements while prohibiting any lateral deformations. This configuration simulates the boundary conditions that facilitate the accurate representation of the soil's response to vertical loading. The interface between the steel ring wall and the heat-resistant concrete is established as a fixed constraint to simulate the perfect bonding between these two components, ensuring that they behave monolithically under load. The remaining structural elements are assigned free boundary conditions, allowing for unconstrained deformation in all directions, which is

critical for capturing the true behavior of the structure under the influence of complex loading scenarios.

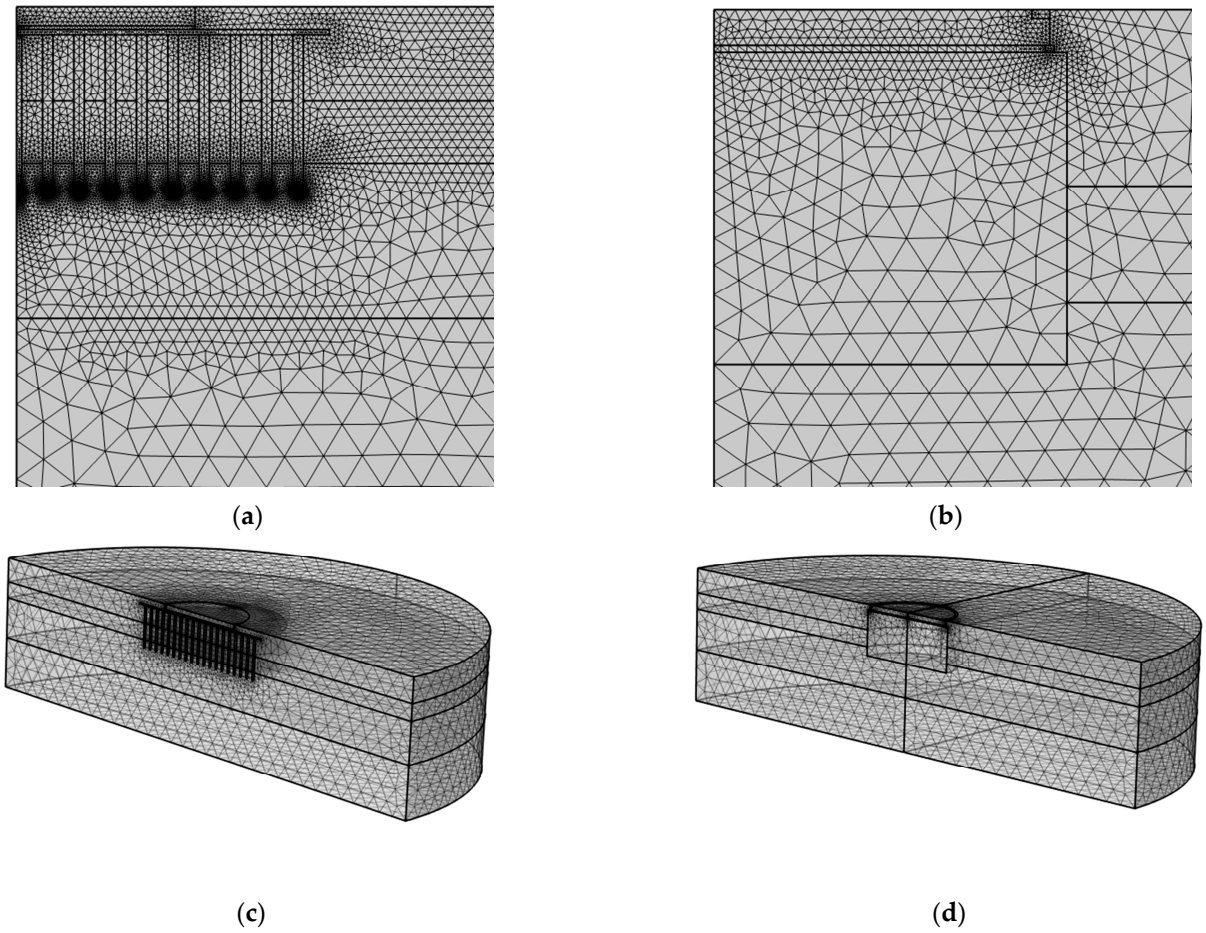


Figure 2. Geometric model and grid division. (**a**) Case 2; (**b**) Case 3; (**c**) Case 2 in 3D; (**d**) Case 3 in 3D.

3.6.2. Temperature Field Setting

The operational temperature range of the high-temperature tank is specified as 525 °C to 535 °C, with a design temperature threshold set at 550 °C. For the purposes of this analysis, it is postulated that the temperature of the high-temperature tank is directly imparted to the surface of the foundation, with negligible heat loss occurring during the transfer process. Consequently, the temperature at the upper surface of the foundation is prescribed at 550 °C. The temperature at the foundation's base is stipulated at 80 °C, attributable to the presence of a ventilation pipe embedded within a fine gravel layer beneath the foundation. This infrastructure is instrumental in facilitating airflow and heat dissipation, thereby maintaining a lower temperature at the foundation's base. The bottom, sides, and top of the foundation soil are hypothesized to be at an ambient temperature of 20 °C, which is considered a standard reference for the environmental conditions surrounding the foundation.

3.6.3. Load Setting

In this engineering project, the construction site for the molten salt storage tank is situated in a region that is advantageous for seismic resistance in building structures, with an annual mean wind velocity of 1.5 m/s. Moreover, the molten salt storage tank does not classify as a slender high-rise structure. Consequently, the impacts of dynamic loads, including seismic and wind loads, have not been factored into the analysis. In accordance with the design specifications for this molten salt storage tank, the tank's load must be

calculated based on the volume of molten salt required for a 12 h thermal energy storage duration. Specifically, the thermal storage capacity for each molten salt tank should be calibrated to accommodate at least 29,500 metric tons of molten salt to meet the foundational load requirements for the molten salt storage tank. The mass of the tank structure, inclusive of its ancillary components, is quantified at 700 metric tons. The base diameter of the tank is delineated as 38.7 m. Under the assumption that the load exerted by the tank is uniformly distributed across the upper surface of the foundation, the areal load imparted to the foundation's upper surface can be derived as 252 kN/m^2.

3.7. Grid Subdivision

Owing to the significant disparity in dimensions between the foundation and the foundation soil, a balance between computational fidelity and computational expense must be achieved. To this end, the mesh discretization of the base model is executed utilizing a method of local mesh refinement. Specifically, in regions proximate to the foundation that exhibit abrupt geometric discontinuities or areas of stress concentration, the grid cell size is meticulously reduced to an exceedingly fine resolution. Conversely, the grid cell size for the foundation soil is adjusted to a larger granularity, thereby facilitating a more rapid convergence of the simulation results towards a stable equilibrium. Ultimately, the fully discretized mesh for the traditional foundation comprised 6338 volumetric cells and 754 boundary cells. In the case of the composite foundation in conjunction with the traditional foundation, the complete mesh encompassed 9165 volumetric cells and 1268 boundary cells. The pile raft foundation combined with the traditional foundation was discretized into 8269 volumetric cells and 1053 boundary cells (refer to Figure 2).

3.8. Geological Stress Balance

In the field of geotechnics, foundation models are typically derived from geometric models that account for post-deformation configurations. Geological materials and structures are frequently subjected to in situ stresses in practical scenarios, which can originate from gravitational forces, tectonic movements, and pore water pressures, among other geodynamic factors. Conducting an equilibrium analysis of geological stresses is instrumental in replicating these realistic boundary conditions, thereby endowing the soil with pre-existing stress states without the manifestation of strain. This foundation model, which incorporates the balance of geological stresses, primarily considers the influence of the gravitational field. Initially, a gravitational field is applied to the foundation model to ascertain the internal stress distribution. Subsequently, the computational results are retrieved via the withsol function, which facilitates the superposition of the resultant stress field onto the foundation model as an external stress. This process effectively drives the foundation model towards an equilibrium state reflective of the prevailing geological stress conditions.

3.9. Calculation of Cases

A uniform load of 252 kN/m^2 was imposed on the uppermost layer of the traditional foundation, with the temperature at the foundation's summit calibrated to 550 °C and the temperature at its base maintained at 80 °C (referred to as Case 1). To address the depth and thickness of the underlying low-bearing-capacity silty clay stratum within the foundation soil, the traditional foundation was augmented with immersed pipe gravel piles to create a composite foundation. Subsequently, a uniform load of 252 kN/m^2 was applied to the top of the foundation, with the temperature at the top set to 550 °C and the bottom to 80 °C (referred to as Case 2). In conjunction with the stress conditions prevalent at the tank foundation, a flat plate raft foundation measuring 1 m in thickness with a radius of 18 m was designed. Beneath this raft foundation, prefabricated piles were installed, with a pile length of 15 m and a pile diameter of 0.6 m. The piles were arranged in a square pattern with a spacing of 3.5 m between them. A uniform load of 252 kN/m^2 was then applied to the foundation's top surface, with the temperature at the top set to 550 °C and the bottom to

80 °C (referred to as Case 3). The analysis focuses on the settlement deformation and temperature distribution within the tank foundations under thermo-mechanical coupling effects. The calculations of cases are shown in Table 3.

Table 3. Calculation cases.

Cases	Calculation Condition
Case 1	Traditional foundation + 252 kN/m^2 uniformly distributed load + 550 °C at top of foundation + 80 °C at bottom of foundation
Case 2	Composite foundation + traditional foundation + 252 kN/m^2 uniformly distributed load + 555 °C at top of foundation + 80 °C at bottom of foundation
Case 3	Pile raft foundation + traditional foundation + 252 kN/m^2 uniformly distributed load + 555 °C at the top of foundation + 80 °C at the bottom of foundation

4. Case Analyses

4.1. Analysis of the Traditional Foundation

4.1.1. Temperature Distribution

The temperature distribution across the foundation is depicted in Figure 3a. Analysis of this figure reveals a significant reduction in the temperature of the foundation soil at the base subsequent to the implementation of heat dissipation strategies at the foundation's lower regions. This observation underscores the efficacy of the heat dissipation interventions [10]. The mean temperature within the lightweight aggregate layer was recorded at 314.5 °C, with an average base temperature of 117.5 °C. The peak temperature, reaching 550 °C, was identified at the central region of the foundation's upper surface, whereas the nadir temperature, at 86.4 °C, was observed at the lower periphery of the lightweight aggregate layer (as illustrated in Figure 4a). This indicates a temperature gradient of 432.5 °C across the 1.25 m thickness of the lightweight aggregate layer, equating to a temperature reduction of 346 °C per unit length at the foundation, underscoring the superior insulating properties of the lightweight aggregate. This finding corroborates the research conducted by Zhou H. et al. [26]. The mean temperature of the heat-resistant concrete was determined to be 404.2 °C. The temperature extremes were 550 °C at the maximum and 155 °C at the minimum. For the concrete piers at the base, the mean temperature was 80.3 °C, with a maximum of 83.2 °C and a minimum of 71.3 °C, which are within the acceptable temperature limits for concrete as per the standards outlined in reference [23]. The temperature within the foundation is maintained within the material's permissible range [37–39]. The thermal influence extends to a depth of 5 m and a radius of 18 m. Consequently, the temperature field distribution of the storage tank foundation remains within a controlled and rational ambit.

4.1.2. Settlement Deformation

The vertical displacement distribution of the foundation model is delineated in Figure 5a. Analysis of this figure reveals that the maximum settlement, amounting to 478 mm, occurs at the foundation's central upper surface, with a central compression of the foundation itself being 30 mm and the underlying soil compression being 448 mm. The soil surface displacement adjacent to the foundation is recorded at 4.37 mm, indicative of a marginal uplift of the soil surface next to the foundation, with an uplift value of 4.37 mm. In deference to the petrochemical steel tank foundation and foundation design codes pertaining to tank foundation deformation criteria, the settlement should not exceed 0.009 times the diameter of the tank's base circle [40,41]. Consequently, the allowable settlement threshold is calculated as 0.009 × tank bottom diameter = 348.3 mm. It is evident that the traditional foundation's settlement exceeds this threshold, thus failing to satisfy the stipulated requirements.

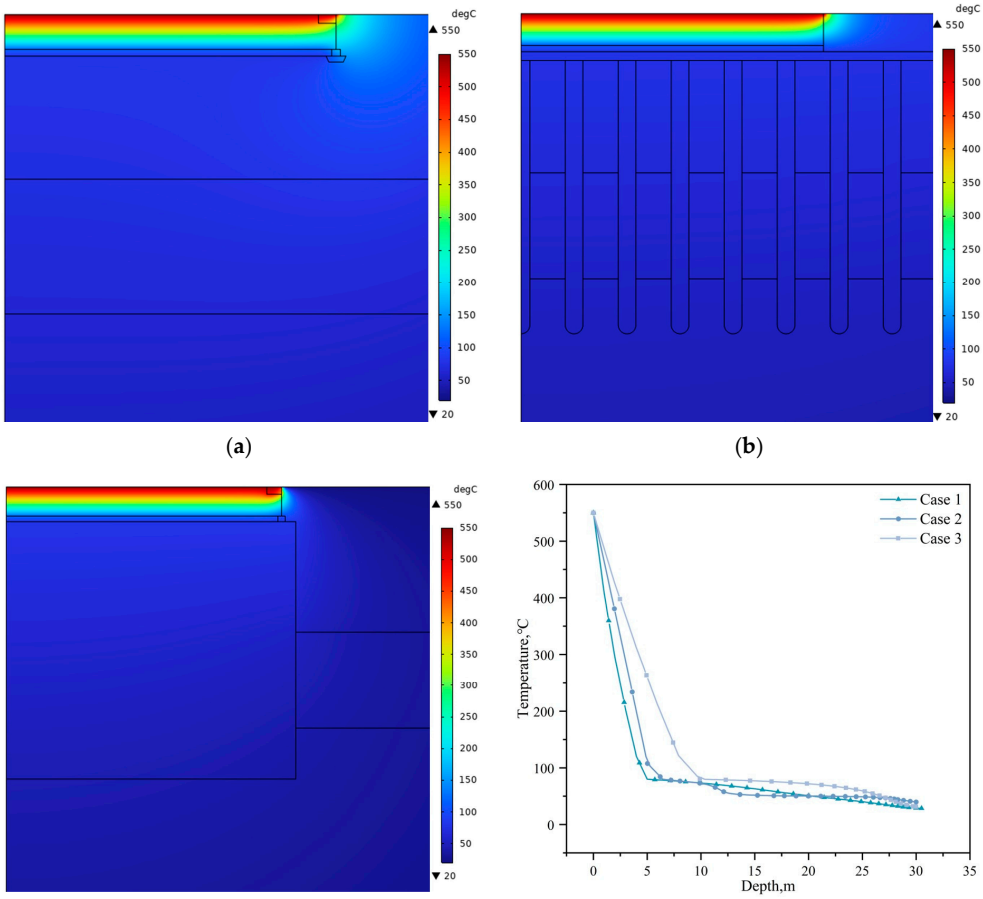


Figure 3. Temperature distribution. (**a**) Case 1; (**b**) Case 2; (**c**) Case 3; (**d**) Temperature variations in the center of the foundation.

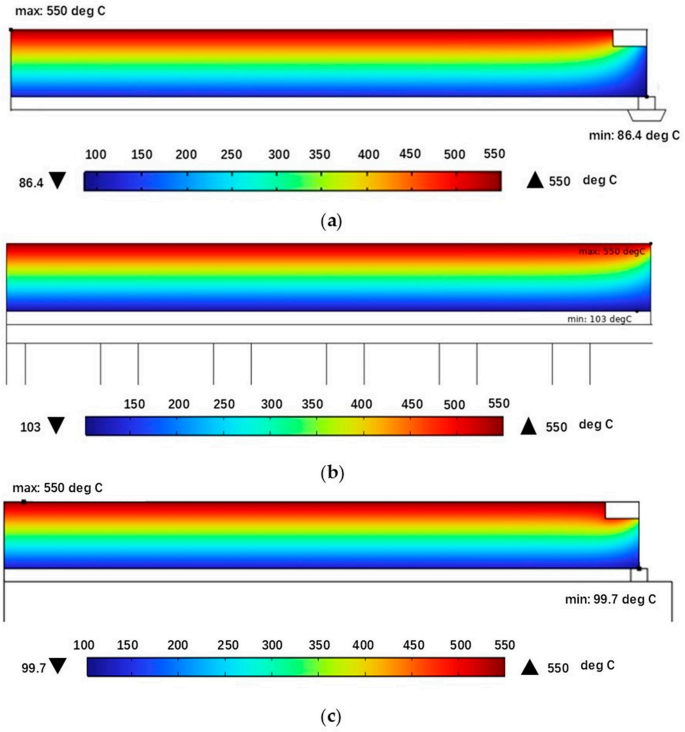


Figure 4. Temperature distribution of lightweight aggregate layer. (**a**) Case 1; (**b**) Case 2; (**c**) Case 3.

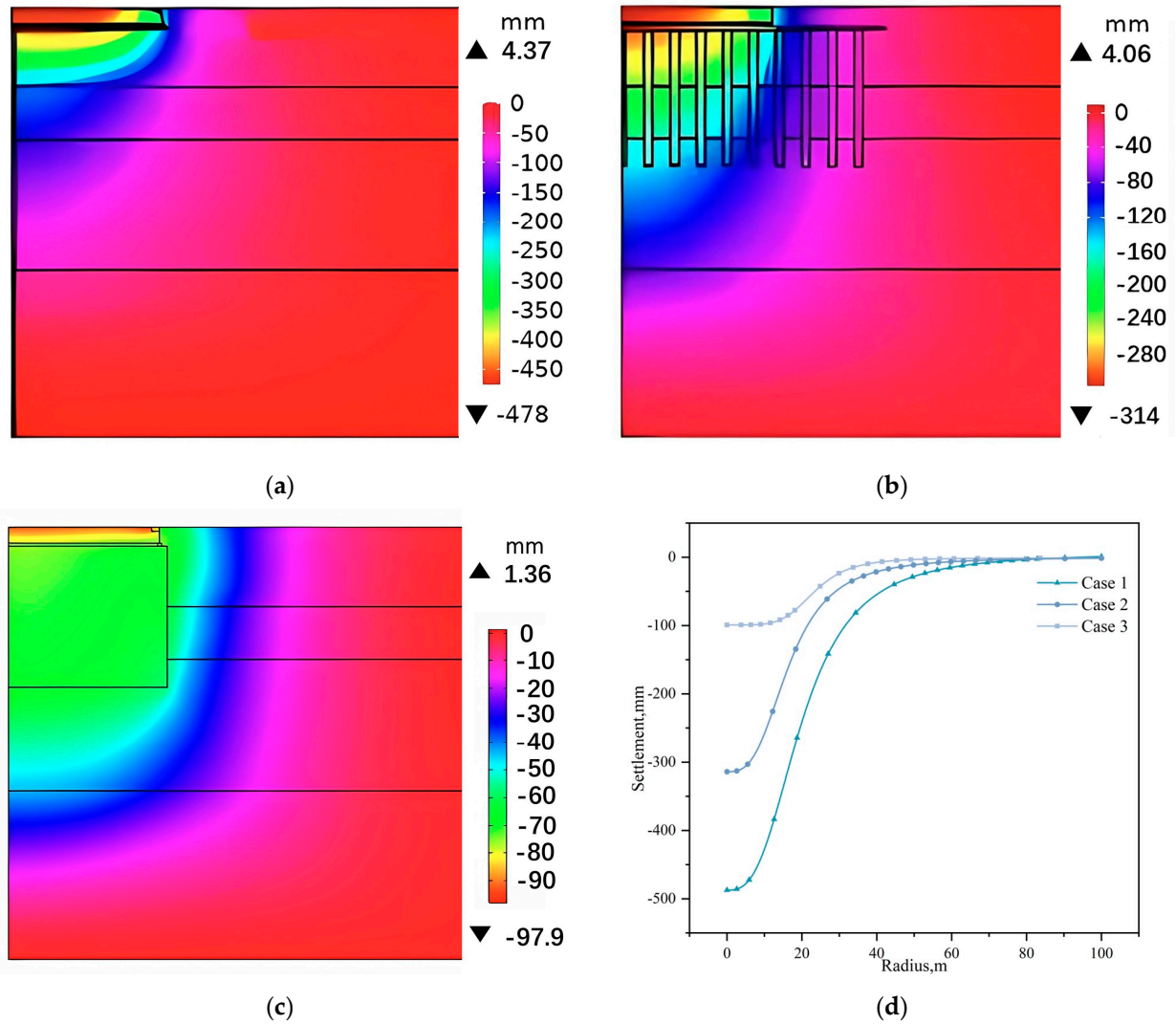


Figure 5. Settlement distribution of the foundation. (**a**) Case 1; (**b**) Case 2; (**c**) Case 3; (**d**) Settlement variations on the top surface of the foundation.

4.1.3. Equivalent Stresses in Steel Ring Wall and Concrete

The distribution of equivalent stress across the steel ring wall of the foundation is delineated in Figure 6a. Concurrently, the equivalent stress distribution within the concrete is depicted in Figure 6b. A thorough examination of these illustrations reveals that the peak stress experienced by the steel ring wall attains a magnitude of 325 MPa. However, the yield strength of the steel ring wall, which is composed of Q355B steel with a thickness of 30 mm, is significantly reduced under elevated temperature conditions. Drawing upon the empirical data presented by Yang C.J. et al., who investigated the temperature alterations in mechanical parameters post-exposure to high temperatures in Q355 steel [42], and the research conducted by Wang W.Y. et al., which focused on the mechanical property indices of high-strength steel at and subsequent to high temperatures [43], it is evident that at a temperature threshold of 550 °C, the yield strength of Q355B steel is approximately 230 MPa. Consequently, the steel ring wall is anticipated to undergo plastic deformation. In contrast, the maximum stress within the concrete is recorded at 815 kPa. The design value for the axial compressive strength of C30 concrete under standard conditions is 14.3 MPa. However, this value is reduced to 70% of its original magnitude under high-temperature scenarios, as reported in the literature [44,45], equating to a revised value of 10 MPa. Given this adjusted compressive strength, the concrete is not expected to exhibit yield behavior under the specified thermal conditions.

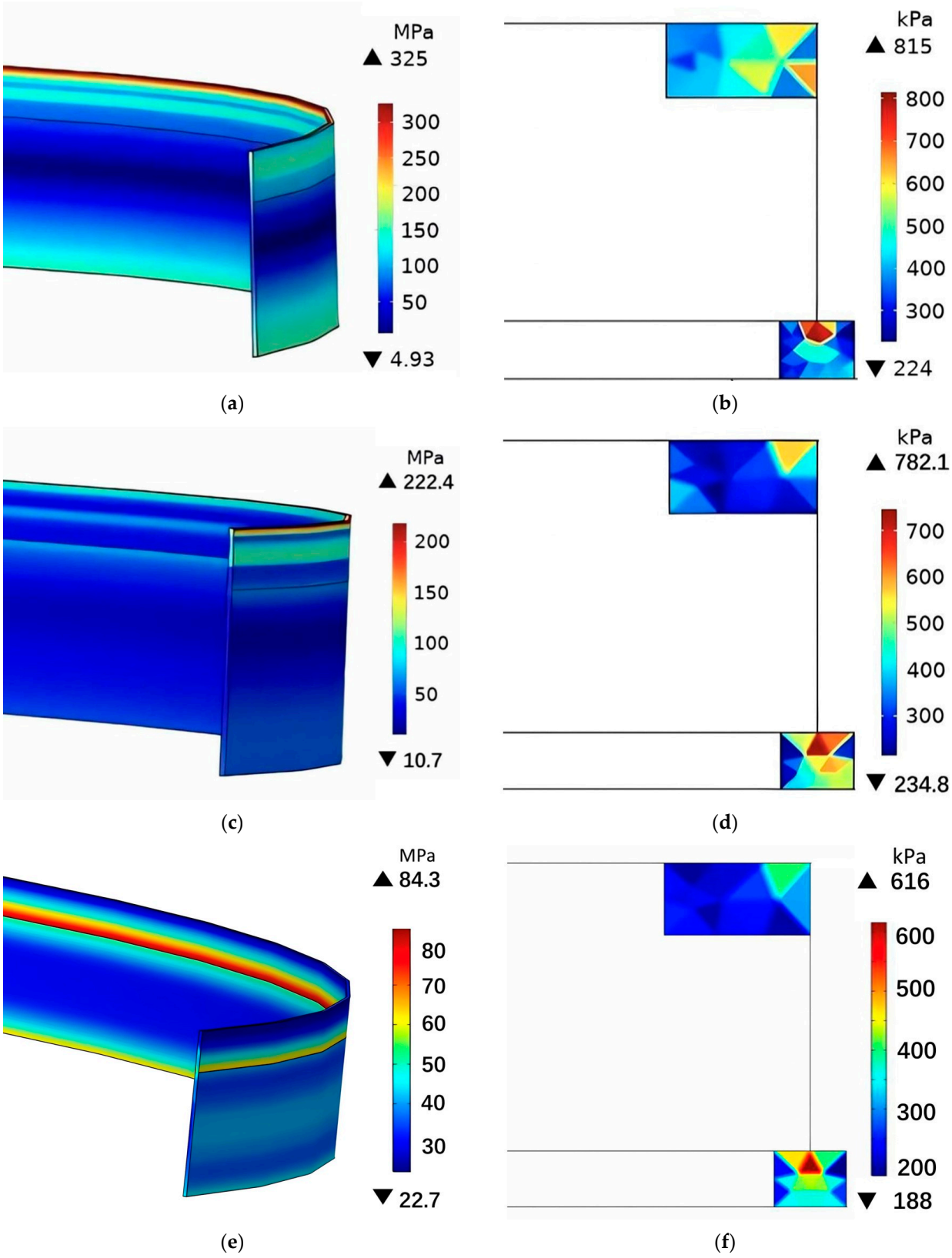


Figure 6. Distribution of equivalent stress. (**a**) Stress of steel ring wall in case 1; (**b**) Stress of concrete in case 1; (**c**) Stress of steel ring wall in case 2; (**d**) Stress of concrete in case 2; (**e**) Stress of steel ring wall in case 3; (**f**) Stress of concrete in case 3.

4.2. Analysis of the Composite Foundation in Conjunction with the Traditional Foundation

4.2.1. Temperature Distribution

The temperature profile of the foundation is illustrated in Figure 3b. Analysis of the temperature distribution reveals a significant reduction in the temperature of the foundation soil at the base following the application of heat dissipation techniques at the foundation's lowermost portion [10]. The lightweight aggregate layer exhibited an average temperature of 326.3 °C, while the average temperature at the lightweight aggregate layer's base was recorded at 107.3 °C. The temperature extremities were characterized by a maximum of 550 °C and a minimum of 103 °C, as detailed in Figure 4b. Furthermore, the temperature distribution within the gravel pile indicated a maximum temperature of 77.7 °C and a minimum of 45.6 °C. These data confirm that the foundation's temperature is effectively managed within the material's acceptable thermal limits [37–39]. The depth of thermal influence within the foundation soil is determined to be 6.2 m, with a radius of influence measuring 24 m. The temperature field distribution surrounding the storage tank foundation is meticulously controlled, ensuring it remains within a predefined and reasonable range, thereby maintaining the structural integrity and performance criteria of the foundation system.

4.2.2. Settlement Deformation

The distribution of vertical displacement within the foundation model is presented in Figure 5b. Upon meticulous analysis of the graphical data, the maximum recorded settlement measures 314 mm, occurring at the central region of the foundation's upper surface. This settlement is attributed to a compressive deformation of 26 mm at the foundation's central core and a corresponding compression of 288 mm at the core of the underlying foundation soil. The displacement of the foundation soil surface in proximity to the foundation is quantified at 4.06 mm, indicative of a marginal, upward movement, or uplift, of the soil surface adjacent to the foundation by a value of 4.06 mm. In deference to the petrochemical steel tank foundation and the foundation design code pertaining to tank foundation deformation criteria, which stipulates that the foundation settlement should not exceed 0.009 times the diameter of the tank's basal circular plane [40,41], the permissible settlement threshold is calculated to be 0.009 × tank bottom diameter = 348.3 mm. Consequently, the observed settlement complies with the prescribed design specifications.

4.2.3. Equivalent Stresses in Steel Ring Wall and Concrete

The distribution of equivalent stress within the foundation's steel ring wall is delineated in Figure 6c. Similarly, the equivalent stress profile of the concrete component is presented in Figure 6d. An analysis of these distributions indicates that the steel ring wall endures a maximum stress of 222.4 MPa. Considering the steel ring wall is composed of Q355B steel with a nominal thickness of 30 mm, its yield strength is adversely affected at elevated temperatures. Referring to the investigative work by Yang C.J. et al. on the thermal modifications to the mechanical properties of Q355 steel post-exposure to high temperatures [42] and the concurrent research by Wang W.Y. et al., which examines the mechanical property indices of high-strength steel under and subsequent to high-temperature conditions [43], it is established that at a temperature of 550 °C, the yield stress of Q355B steel is approximately 230 MPa. Consequently, the steel ring wall is anticipated to remain in the elastic regime and not to undergo plastic deformation. Furthermore, the concrete component registers a maximum stress of 782.1 kPa. The design axial compressive strength for C30 concrete is cited as 14.3 MPa, which, according to referenced literature [44,45], is attenuated to 70% of its standard value under high-temperature scenarios, translating to a reduced threshold of 10 MPa. Therefore, the concrete is also projected to maintain its elastic behavior and not to exhibit yielding under the specified conditions.

4.3. Analysis of the Pile Raft Foundation in Conjunction with the Traditional Foundation

4.3.1. Temperature Distribution

The temperature distribution of the foundation is elucidated in Figure 3c. A meticulous analysis of this depiction indicates a significant reduction in the temperature of the foundation soil at the base subsequent to the implementation of thermal dissipation strategies at the foundation's lower extremity [10]. The lightweight aggregate layer exhibits an average temperature of 326.3 °C, with the bottom region averaging at 107.3 °C. The temperature extremes are delineated by a maximum of 550 °C and a minimum of 99.7 °C, as presented in Figure 4c. The heat-resistant concrete maintains an average temperature of 494.2 °C, with thermal maxima and minima reaching 550 °C and 388 °C, respectively. The substructure's concrete pier exhibits a more moderate temperature range, with an average of 81.7 °C, a maximum of 84 °C, and a minimum of 80 °C, all of which are within the prescribed limit of not surpassing 90 °C in accordance with the specifications outlined in reference [23]. Furthermore, the equivalent soil body's average temperature is recorded at 57.9 °C, with a maximum of 83.4 °C and a minimum of 37.1 °C. These temperature parameters are well within the acceptable tolerance levels for the materials in question [37–39]. The depth of thermal influence within the foundation soil extends to 10 m, with a radial extent of influence of 20 m. The temperature field distribution of the storage tank foundation is meticulously regulated, ensuring that it remains within a predefined and reasonable range. This stringent temperature control is essential for preserving structural integrity and ensuring the longevity of the foundation.

4.3.2. Settlement Deformation

The vertical displacement distribution of the foundation model is depicted in Figure 5c. Analysis of the displacement data reveals that the maximum settlement, amounting to 97.9 mm, occurs at the centroid of the foundation's upper surface. This settlement is attributed to a compressive deformation of 13.5 mm at the foundation's central region and a subsequent compression of 84.4 mm at the core of the underlying soil. The displacement of the soil surface adjacent to the foundation is recorded at 1.36 mm, indicating a marginal, upward adjustment, or uplift, of the soil surface by this magnitude. In accordance with the petrochemical steel tank foundation and the foundation design code pertaining to deformation criteria for tank foundations, specifically, that the foundation settlement should not exceed 0.009 times the diameter of the tank's basal circular plane [40,41], the permissible settlement threshold is calculated to be 0.009 × tank bottom diameter = 348.3 mm. Consequently, the observed settlement is found to be in compliance with the design specifications, thereby ensuring the structural stability and performance of the foundation in accordance with the established engineering standards.

4.3.3. Equivalent Stresses in Steel Ring Wall and Concrete

The distribution of equivalent stresses within the foundation's steel ring wall is delineated in Figure 6e. Concurrently, the equivalent stress profile of the concrete component is portrayed in Figure 6f. Upon analysis, it is observed that the steel ring wall experiences a maximum stress of 84.3 MPa. Given the steel ring wall is composed of Q355B steel with a thickness of 30 mm, its yield stress is significantly reduced under elevated temperature conditions. Referring to the investigative work by Yang C.J. et al. on the thermal modifications to the mechanical properties of Q355 steel post-exposure to high temperatures [42] and the concurrent research by Wang W.Y. et al., which examines the mechanical property indices of high-strength steel under and subsequent to high-temperature conditions [43], it is established that at a temperature of 550 °C, the yield stress of Q355B steel is approximately 230 MPa. Consequently, the steel ring wall is anticipated to remain in the elastic regime and not to exhibit yield behavior. Furthermore, the concrete component registers a maximum stress of 616 kPa. The design axial compressive strength for C30 concrete is cited as 14.3 MPa, which, according to referenced literature [44,45], is attenuated to 70% of its standard value under high-temperature conditions, translating to a reduced threshold of

10 MPa. Therefore, the concrete is also projected to maintain its elastic behavior and not to yield under the conditions.

4.4. Comparative Analysis of Cases

The temperature distribution of the foundation soil is shown in Figure 7, and the temperature variation curves at different depths from the base of the foundation are shown in Figure 7d. Incorporating data obtained from simulation calculations, we have derived a set of mathematical models through nonlinear surface fitting to predict the temperature at any point within the foundation soil beneath the foundation. For traditional foundation, the mathematical models derived from nonlinear surface fitting are as follows:

$$T = 87.45 - 1.94R - 3.45D + 0.072R \bullet D \quad (4)$$

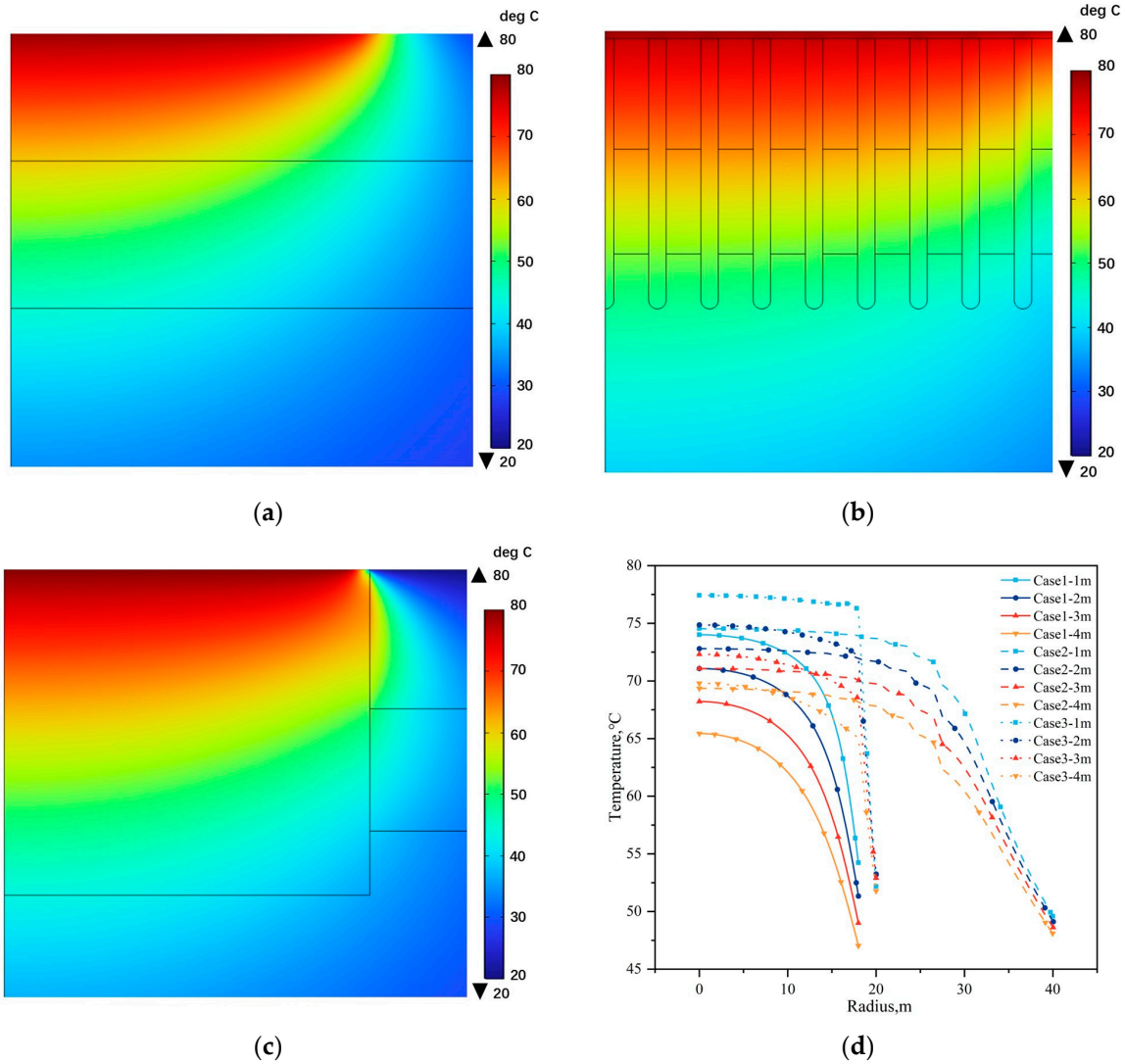


Figure 7. Soil temperature distribution of the foundation. (**a**) Case 1; (**b**) Case 2; (**c**) Case 3; (**d**) Temperature variations at different depths from the bottom of the foundation.

For the composite foundation in conjunction with the traditional foundation model, the mathematical models derived from nonlinear surface fitting are as follows:

$$T = 76.51 - 0.54R - 1.99D + 0.021D^2 \quad (5)$$

For the pile raft foundation in conjunction with the traditional foundation model, the mathematical models derived from nonlinear surface fitting are as follows:

$$T = 14.96 + 76.29 \bullet e^{\left(\frac{-R}{27.26}\right)} \bullet e^{\left(\frac{-D}{21.79}\right)} \quad (6)$$

In which T represents the temperature of the foundation soil, in degrees Celsius (°C); R represents the distance from the center of the foundation, in meters (m); and D represents the depth from the base of the foundation, in meters (m).

This lays an important theoretical foundation and offers a certain reference for future predictions of foundation soil temperature.

A comparison of the traditional foundation at the same depth reveals that the temperature is slightly higher for both the composite foundation in conjunction with the traditional foundation model and the pile raft foundation in conjunction with the traditional foundation model. The data demonstrate that the temperature differential between any two points of the foundation soil of the traditional foundation is higher than that observed between any two points of the other two cases at the same location, within the temperature tolerance range of the foundation soil. In other words, the thermal conductivity of traditional foundation soils is relatively high, which leads to suboptimal insulative properties and, consequently, a significant loss of energy. The composite foundation in conjunction with the traditional foundation mode and the pile raft foundation in conjunction with the traditional foundation mode exhibit reduced thermal conductivity. This enhancement in thermal resistance results in superior thermal insulation and, consequently, a reduction in energy dissipation. Additionally, the pile raft foundation in conjunction with the traditional foundation mode exhibits the most effective thermal insulation performance. The variation of temperature with depth at the center of the foundation is shown in Figure 3d. The temperature profile exhibits a near-linear relationship with depth, with the rate of temperature change abruptly moderating at a threshold depth. This phenomenon implies the presence of a finite depth of influence for temperature, and comparative assessments reveal the differences are minimal in this depth of influence between traditional foundations and the composite-foundation-traditional-foundation hybrid system. The settlement at the uppermost surface of the foundation exhibits a variability that is contingent upon the radial distance from the foundation's centroid, as delineated in Figure 5d. The settlement progressively diminishes from the central axis towards the periphery of the foundation, asymptotically approaching zero beyond a radius of 20 m. This trend infers that the surcharge imposed by the tank exerts an influence over a finite areal extent, with negligible impact on the settlement of the foundation and the adjacent soil beyond this threshold. Furthermore, the settlement of the pile raft foundation in conjunction with the traditional foundation mode is markedly mitigated in comparison to the other two cases.

In the context of geotechnical engineering, traditional foundation systems exhibit diminished adaptability when confronted with intricate geological conditions. The subsidence of such foundations under complex geological strata is considerably more pronounced compared to those situated in general geological settings, often exceeding the stipulated design specifications. The integrity of the steel ring wall under elevated temperature conditions is compromised, with a significant reduction in their load-bearing capacity. This is particularly evident when the stress within the steel ring wall surpasses its yield stress, indicating a propensity for structural failure in traditional foundations when subjected to the complexities of diverse geological formations. Such failures can impede the operational efficacy of tank equipment and potentially jeopardize the overall integrity of the storage tank. Consequently, for molten salt storage tanks to be viable in environments characterized by complex geological conditions, it is imperative that the foundation design be re-engineered. This redesign must ensure that the settlement and deformation are maintained within acceptable limits and that the bearing capacity is adequate to meet the functional demands of the storage system.

Upon the implementation of geotechnical remediation measures, the foundation soil is transformed into a composite foundation. This composite foundation, when integrated with a traditional foundation, exhibits enhanced adaptability in the presence of complex geological conditions. The settlement is significantly mitigated by 164mm, or 34.3%, in comparison to the traditional foundation, thereby aligning with the design specifications. In contrast to the traditional foundation, the peak stress experienced by the steel ring wall is diminished by 102.6 MPa, while the maximum stress in the concrete is reduced by 32.9 kPa. The strength of the steel ring wall and concrete is attenuated under high-temperature conditions; however, the post-discount maximum stress of both the steel ring wall and concrete in the foundation remains below the yield stress of the steel plate. This indicates that the composite foundation combined with the traditional foundation maintains its structural integrity and does not exhibit yielding behavior, thus satisfying the load-bearing requirements. Although the foundation temperature is regulated within the material's permissible range, there is an increase in the average temperature of the lightweight aggregate layer by 11.8 °C, with a minimum temperature rise of 16.6 °C when compared to the traditional foundation. This suggests a moderate reduction in the thermal insulation efficacy of the lightweight aggregate layer, potentially attributable to the disruption of the original integrity of the foundation soil post-treatment. Further investigative research is warranted to elucidate these observations and to optimize the foundation design for complex geological settings. Furthermore, the foundation soils exhibit enhanced insulative properties, resulting in diminished energy dissipation within the permissible temperature range of the foundation soils.

The integration of a pile raft foundation with a traditional foundation demonstrates exceptional adaptability in the context of complex geological challenges. This hybrid foundation system significantly outperforms both the traditional foundation and the composite foundation combined with a traditional foundation in terms of settlement reduction, aligning with the stringent design criteria. In comparison to the traditional foundation, the settlement is markedly decreased by 380.1mm, representing a 79.5% reduction. Concurrently, the maximum stress experienced by the steel ring wall is alleviated by 240.7 MPa, and the peak stress in the concrete is diminished by 199 kPa. When juxtaposed with the composite foundation augmented by a traditional foundation, the settlement is still reduced by 216.1mm, with the steel ring wall's maximum stress reduced by 138.1 MPa and the concrete's maximum stress by 166.1 kPa. At elevated temperatures, the strength of the steel ring wall and concrete is subject to a reduction factor. Post-adjustment, the maximum stresses within the foundation's steel ring wall and concrete remain below their yield stress, signifying that the material will maintain its elastic behavior without yielding. This affirms that the load-bearing capacity of the pile raft foundation in conjunction with the traditional foundation is adequate to fulfill the structural demands. The foundation's temperature is meticulously regulated, ensuring it remains within the material's permissible tolerance range, thereby safeguarding the integrity and performance of the foundation system under the influence of high temperatures. In comparison to the traditional foundation, the mean temperature augmentation of the lightweight aggregate layer was observed to be 15.8 °C, with the lowest temperature increment recorded at 13.3 °C, indicating a moderate diminishment in the thermal insulation efficacy of the lightweight aggregate layer. Nevertheless, when contrasted with the other two cases, the foundation soil exhibited superior thermal insulation properties and minimal energy dissipation within the permissible temperature range of the foundation soils.

5. Conclusions

In the context of complex geology, the engineering challenges associated with tank foundations are manifold. The potential for uneven settlement, cracking, and even destabilization damage is heightened when the foundations are subjected to thermal and force cycles. Addressing this engineering issue, this study integrates the design of a storage tank for a tower-type solar thermal power station in Xinjiang. The paper establishes a

two-dimensional axisymmetric model of the tank foundation using COMSOL Multiphysics. Material parameters are set based on the actual measured data obtained from site reconnaissance. The failure criteria for the materials are the Drucker–Prager criterion and the Bresler–Pister criterion. Subsequently, loads and temperature fields are applied to the tank foundation to simulate the actual working condition of a molten salt storage tank. Numerical simulation analysis is conducted on the settlement deformation and temperature distribution of the foundation under the coupled action of heat and load. Two foundation design methods are proposed: a composite foundation combined with a traditional foundation and a pile raft foundation combined with a traditional foundation. The research conclusions are as follows:

- In the context of complex geological conditions, traditional foundations exhibit diminished adaptability. The settlement of traditional foundations in such geologically complex contexts undergoes a significant increment relative to more generic geological settings, and the load-bearing capacity of the steel ring wall is found to be inadequate to fulfill the necessary engineering demands.
- The composite foundation, in conjunction with the traditional foundation mode, demonstrates enhanced adaptability when encountering complex geology. Relative to the traditional foundation, this model exhibits a reduction in settlement by 164 mm or 34.3%, and it successfully satisfies the requisite bearing-capacity criteria. A commensurate reduction in the thermal insulation capacity of the lightweight aggregate layer is observed. However, the foundation soil presents more robust thermal insulation attributes, coupled with a decrease in energy loss.
- The pile raft foundation, in conjunction with the traditional foundation mode, manifests superior adaptability within the context of intricate geology. The settlement exhibits a pronounced decline when compared to both the traditional foundation and the composite foundation in conjunction with the traditional foundation. In comparison to the traditional foundation, the settlement is diminished by 380.1mm, representing a 79.5% reduction. In comparison to the composite foundation in conjunction with the traditional foundation mode, the settlement is reduced by 216.1mm. Furthermore, the bearing capacity is in accordance with the specified requirements. A commensurate reduction in the thermal insulation capacity of the lightweight aggregate layer is observed. Relative to the other two cases, the foundation soil demonstrates the most effective thermal insulation and the lowest degree of energy loss.
- Incorporating data obtained from simulation calculations, a set of mathematical models has been derived through nonlinear surface fitting to predict the temperature at any point within the foundation soil beneath the foundation.

This study provides two potential foundation design approaches for molten salt storage tanks facing complex geological conditions. It offers both qualitative and quantitative analyses of the settlement deformation and temperature distribution of the foundation under the coupled action of heat and load, serving as a reference for the design of tank foundations under similar geological conditions in the future.

Author Contributions: Conceptualization, S.Z. and X.L.; methodology, Y.L. and H.S.; software, Y.L. and H.S.; validation, Y.L., H.S. and X.K.; formal analysis, Y.L. and H.S.; investigation, S.Z. and X.L.; resources, S.Z. and X.L.; data curation, Y.L. and H.S.; writing—original draft preparation, Y.L. and H.S.; writing—review and editing, X.K.; visualization, X.K.; project administration, X.K. All authors have read and agreed to the published version of the manuscript.

Funding: This project "Research on Key Design Technologies for High Temperature Molten Salt Tank Foundation" was funded by Shandong Electric Power Engineering Consulting Institute Co., Ltd.

Data Availability Statement: The data presented in this paper are supported by finite element simulation results and the above references.

Acknowledgments: The authors would like to thank the technical support from Shandong Electric Power Engineering Consulting Institute Co. and the theoretical guidance from the College of Civil Engineering, Hunan University.

Conflicts of Interest: Authors Shezhou Zhu and Xu Li were employed by the company Shandong Electric Power Engineering Consulting Institute Co., Ltd. The remaining authors declare that the research was conducted in the absence of any commercial or financial relationships that could be construed as a potential conflict of interest. The funding sponsors had no role in the design of the study; in the collection, analyses, or interpretation of data; in the writing of the manuscript, and in the decision to publish the results.

References

1. Asif, M.; Muneer, T. Energy supply, its demand and security issues for developed and emerging economies. *Renew. Sustain. Energy Rev.* **2007**, *11*, 1388–1413. [CrossRef]
2. U.S. Energy Information Administration. U.S. EIA: International Energy Outlook 2021: With projections to 2050-Summary. *VGB PowerTech* **2021**, *101*, 81–84.
3. Zhang, H.L.; Baeyens, J.; Degrève, J.; Cacères, G. Concentrated solar power plants: Review and design methodology. *Renew. Sustain. Energy Rev.* **2013**, *22*, 466–481. [CrossRef]
4. Pitie, F.; Zhao, C.Y.; Baeyens, J.; Degreve, J.; Zhang, H.L. Circulating fluidized bed heat recovery/storage and its potential to use coated phase-change-material (PCM) particles. *Appl. Energy* **2013**, *109*, 505–513. [CrossRef]
5. Zhang, J.P.; Zhou, Q. Overview of Solar Thermal Power Generation Technology and Its Development. *iEnergy* **2023**, *45*, 44–52.
6. China Will Continue to Promote the Green and Low-Carbon Transition of Energy in This Year. Available online: https://www.gov.cn/yaowen/shipin/202403/content_6941122.htm (accessed on 23 March 2024).
7. Zhou, H.; Shi, H. Experimental and numerical investigation of temperature distribution and heat loss of molten salt tank foundation at different scales. *Heat Mass Transf.* **2020**, *56*, 2859–2869. [CrossRef]
8. Zhang, H.L.; Baeyens, J.; Caceres, G.; Degreve, J.; Lv, Y.Q. Thermal energy storage: Recent developments and practical aspects. *Prog. Energy Combust. Sci.* **2016**, *53*, 1–40. [CrossRef]
9. Tian, Y.; Zhao, C.Y. A review of solar collectors and thermal energy storage in solar thermal applications. *Appl. Energy* **2013**, *104*, 538–553. [CrossRef]
10. Wan, Z.J.; Wei, J.J. Evaluation on thermal and mechanical performance of the hot tank in the two-tank molten salt heat storage system. *Appl. Therm. Eng.* **2020**, *167*, 114775. [CrossRef]
11. Gabbrielli, R.; Zamparelli, C. Optimal design of a molten salt thermal storage tank for parabolic trough solar power plants. *J. Sol. Energy Eng.* **2010**, *131*, 041001. [CrossRef]
12. Gasia, J.; Miró, L.; Cabeza, L.F. Review on system and materials requirements for high temperature thermal energy storage. Part 1: General requirements (Review). *Renew. Sustain. Energy Rev.* **2017**, *75*, 1320–1338. [CrossRef]
13. Janz, G.J. *Molten Salts Handbook*; Academic Publisher: New York, NY, USA, 1967.
14. Zhou, H.; Shi, H.; Zhu, Y.F. An experimental investigation of temperature distribution and heat loss in molten salt tanks in concentrating solar power plants. *J. Renew. Sustain. Energy* **2020**, *12*, 1–11. [CrossRef]
15. Wen, J.D.; Alexander, B.; Joachim, G. Electrochemical measurement of corrosive impurities in molten chlorides for thermal energy storage. *J. Energy Storage* **2018**, *15*, 408–414.
16. Gomez-Vidal, J.C.; Morton, E. Castable cements to prevent corrosion of metals in molten salts. *Sol. Energy Mater. Sol. Cells* **2016**, *153*, 44–51. [CrossRef]
17. Muhammad, T.M.; Laurence, P.; Melanie, T.F. Concrete based molten salt storage tanks. *J. Energy Storage* **2023**, *57*, 106151.
18. Wang, W.J.; Zhong, Z.W. Physico-mechanical properties and micromorphological characteristics of graphene oxide reinforced geopolymer foam concrete. *J. Build. Eng.* **2023**, *72*, 106732. [CrossRef]
19. Gómez-Villarejo, R.; Martín, E.I.; Navas, J. Ag-based nanofluidic system to enhance heat transfer fluids for concentrating solar power: Nano-level insights. *Appl. Energy* **2017**, *194*, 19–29. [CrossRef]
20. Zhou, H.; Wang, Z.W.; Zhou, M.X. Experimental measurements and XCT based simulation of effective thermal conductivity of stacked ceramsites in molten-salt tank foundation. *Heat Mass Transf.* **2019**, *55*, 3103–3115. [CrossRef]
21. Torras, S.; Pérez-Segarra, C.D.; Rodríguez, I. Parametric study of two-tank TES systems for CSP plants. *Energy Procedia* **2015**, *69*, 1049–1058. [CrossRef]
22. Zhang, X.M.; Wu, Y.T.; Ma, C.F. Experimental Study on Temperature Distribution and Heat Losses of a Molten Salt Heat Storage Tank. *Energies* **2019**, *12*, 1943. [CrossRef]
23. Rodríguez, I.; Pérez-Segarra, C.D.; Lehmkuhl, O. Modular object-oriented methodology for the resolution of molten salt storage tanks for CSP plants. *Appl. Energy* **2013**, *109*, 402–414. [CrossRef]
24. Schulte-Fischedick, J.; Tamme, R.; Herrmann, U. *CFD Analysis of the Cool down Behaviour of Molten Salt Thermal Storage Systems*; ES 2008; Elsevier: Jacksonville, FL, USA, 2008.
25. Yang, X.P.; Yang, X.X.; Qin, F.G.F.; Jiang, R. Experimental investigation of a molten salt thermocline storage tank. *Int. J. Sustain. Energy* **2016**, *35*, 606–614. [CrossRef]

26. Zhou, H.; Wang, Z.W.; Zhou, M.X. Thermal properties, permeability and compressive strength of highly porous accumulated ceramsites in the foundation of salt tank for concentrate solar power plants. *Appl. Therm. Eng.* **2020**, *164*, 114451. [CrossRef]
27. Xia, Z.; Chen, R.P.; Kang, X. Laboratory characterization and modelling of the thermal-mechanical properties of binary soil mixtures. *Soils Found.* **2019**, *59*, 2167–2179. [CrossRef]
28. Kang, X.; Ge, L. Enhanced series-parallel model for estimating the time-dependent thermal conductivity of fly ash soil mixtures. *Granul. Matter* **2015**, *17*, 579–592. [CrossRef]
29. Kang, X.; Ge, L.; Kang, G.C. Laboratory investigation of the strength, stiffness, and thermal conductivity of fly ash and lime kiln dust stabilised clay subgrade materials. *Road Mater. Pavement* **2015**, *16*, 928–945. [CrossRef]
30. Pacheco, J.E.; Gilbert, R. Overview of recent results of the solar two test and evaluations program. In Proceedings of the ASME International Solar Energy Conference, Maui, HI, USA, 11–15 April 1999.
31. *API Stand 650*; Welded Tanks for Oil Storage, 12th ed. American Petroleum Institute: Washington, DC, USA, 2013.
32. Liang, T.; Mi, Y.W.; Li, Q.Y. Temperature distribution and settlement deformation of molten salt storage tank foundation in a trough type solar thermal power station under multi field coupling. *Build. Tech. Dev.* **2022**, *49*, 120–126.
33. Tian, Q.; Wang, J.P.; Pu, Y.J. Basic research on high-temperature molten salt storage tank based on thermal analysis. *Wuhan Univ. J.* **2017**, *50*, 282–284.
34. Teng, Y.J.; Zhang, Y.J.; Yan, M.L. *Technical Code for Ground Treatment of Buildings*, 5th ed.; China Architecture & Building Press: Beijing, China, 2012.
35. China Academy of Building Research. *Technical Code for Building Pile Foundations*, 3rd ed.; China Architecture & Building Press: Beijing, China, 2008.
36. CnTech Co., Ltd. *COMSOL Multiphysics Manual in Chinese*; CnTech Co., Ltd.: Gumi-si, Republic of Korea, 2008.
37. Tawzia, M.; Javed, A.B.; Asif, H.S. Performance of geopolymer concrete at elevated temperature—A critical review. *Constr. Build. Mater.* **2024**, *420*, 135578.
38. Li, Y.M.; Yu, Z.Z.; Lin, J.L. High-temperature deformation of molded sand and the way of destruction. *J. Shenyang Univ. Technol.* **1992**, *1*, 1–9.
39. Asad, S.A.; Rwayda, K.S.A.-H.; Saif, A. Soft computing models for assessing bond performance of reinforcing bars in concrete at high temperatures. *Innov. Infrastruct. Solut.* **2023**, *8*, 218.
40. Tan, L.J.; Chen, C.J. *Design Specification for Steel Storage Tanks Subgrade and Foundation in Petrochemical Enterprises*, 2nd ed.; China Petrochemical Press: Beijing, China, 2007; pp. 15–18.
41. Sinopec Group. *Code for Design of Steel Tank Foundation*, 1st ed.; China Planning Press: Beijing, China, 2008.
42. Yang, C.J.; Zhang, C.T. Experimental study on mechanical properties of Q355 steel after high temperature water cooling. *Ind. Constr.* **2021**, *51*, 165–170.
43. Wang, W.Y.; Zhang, Y.H.; Li, G.Q. Study of standardized values of mechanical property indexes of high-strength steels at and after high temperatures. *J. Build. Struct.* **2022**, *43*, 130–150.
44. Xu, G.F.; Hang, M.Y. Study on the use of refractory bricks as aggregates for the formulation of heat-resistant concrete. *Sci. Technol. Baotou Steel* **2020**, *46*, 79–82.
45. Song, X.S. Prediction of High-Temperature Mechanical Properties of Concrete Based on Deep Learning Algorithms. *Sichuan Cem.* **2023**, *11*, 7–9.

Disclaimer/Publisher's Note: The statements, opinions and data contained in all publications are solely those of the individual author(s) and contributor(s) and not of MDPI and/or the editor(s). MDPI and/or the editor(s) disclaim responsibility for any injury to people or property resulting from any ideas, methods, instructions or products referred to in the content.